

Analytical Model for the Current Density in the Electrochemical Synthesis of Porous Silicon Structures with a Lateral Gradient

C. A. Ospina-Delacruz^a, V. Agarwal^{a,b,1} and W. L. Mochán^{b,*}

^aCentro de Investigación en Ingeniería y Ciencias Aplicadas (CIICAP-IICBA), Universidad Autónoma del Estado de Morelos (UAEM), Cuernavaca CP 62209, México

^bInstituto de Ciencias Físicas, Universidad Nacional Autónoma de México, Av. Universidad S/N, Col. Chamilpa, 62210 Cuernavaca, Morelos, México

ARTICLE INFO

Keywords:

Porous Silicon

GRIN

Reflectance Spectra.

ABSTRACT

Layered optical devices with a lateral gradient can be fabricated through electrochemical synthesis of porous silicon (PS) using a position dependent etching current density $j(r_{\parallel})$. Predicting the local value of $j(r_{\parallel})$ and the corresponding porosity $p(r_{\parallel})$ and etching rate $v(r_{\parallel})$ is desirable for their systematic design. We develop a simple analytical model for the calculation of $j(r_{\parallel})$ within a prism shaped cell. Graded single layer PS samples were synthesized and their local calibration curves p vs j and v vs j were obtained from our model and their reflectance spectra. The agreement found between the calibration curves from different samples shows that from one sample we could obtain full calibration curves which may be used to predict, design, and fabricate more complex non-homogeneous multilayered devices with lateral gradients for manifold applications.

1. Introduction

Surfaces with a gradient in the refractive index (GRIN) are of importance as they allow the engineering and tuning of the optical phase along their surface, yielding applications such as flat lenses. Furthermore, there are important biological applications which combine topographical features with index of refraction gradients [1]. Preparation of structures with gradients in other properties have also shown their usefulness. As an example, the roughness dependent response of cells has been tested on materials used for applications in medical implants [2]. Gradients have also been employed for several technological applications such as high-yield screening of catalysts, sensing materials and biomolecules [3–5]. Apart from some methods developed by S.E. Fosdick et al. [6], synthesis of Ag-Au alloy gradients on steel and chemical composition gradients of CdS layers on gold electrodes have also been obtained [7, 8]. Among electrochemical methods, changes in the composition and doping density of conducting polymers have been used to produce gradients using Indium Tin Oxide electrodes [9]. Electrochemically induced potential gradients have been shown to catalyze the reactions and gradient doping of polymers [10, 11]. As compared to the above mentioned techniques, a relatively economical, fast and easy approach for the fabrication of gradient materials has been the use of asymmetrical electrode configurations in the electrochemical synthesis of porous silicon [12]. This technique has the additional advantage of being compatible with very-large-scale-integration (VLSI) devices that may be integrated in microelectronic circuits.

Although porous silicon (PS) initially stimulated the interest of the scientific community due to its photo-luminescence in the visible range at room temperature, it has presently been recognized as a multifaceted optical material due to its large surface area, bio-compatibility, ease of fabrication and tunable refractive index. Applications based on porous silicon now cover various fields such as chemical sensors and biosensors [13–15], microelectronics and micro-mechanical systems (MEMS) [16], as well as a range of optical [17] and opto-electronic applications [18–21]. Specifically, the temporal variation of the current density results in a variation of porosity along the depth, allowing the easy fabrication of different kinds [22–25] of 1D dielectric multilayered structures. Although the conventional fabrication of PS yields

*Corresponding author

✉ crisalod@gmail.com (C.A. Ospina-Delacruz); vagarwal@uaem.mx (V. Agarwal); mochan@fis.unam.mx (W.L. Mochán)

ORCID(s): 0000-0002-9609-3031 (C.A. Ospina-Delacruz); 0000-0003-2168-853X (V. Agarwal); 0000-0003-0418-5375 (W.L.

Mochán)

¹On sabbatical leave at ICF-UNAM from CIICAP-UAEM.

laterally homogeneous samples, with invariant structural and optical properties along the surface, another configuration where a Pt pin electrode is placed perpendicular to the silicon wafer, produces porous silicon structures with a lateral gradient in properties such as thickness, pore size and density, and thus, refractive index and optical thickness [26, 27]. The resulting porous surface can have pore sizes ranging from a few nanometers to few micrometers [28]. The range of the dimensions of the pores and the corresponding thickness range on the same chip can be controlled by adjusting the location of the electrode, the anodizing current and the etching time. Different applications have been found for the resulting structures [29]. For example, Sailor's group [12, 29] applied it for the determination of protein size. Additionally, a variation in pH of the solution could gate the trapping/release of bio-molecules at regions with different porosity, a result potentially useful for drug delivery applications given the bio-compatible nature of PS. A similar asymmetric electrode configuration was used to fabricate multilayered optical filters with lateral a gradient [30] and for developing ethanol sensors [12]. Additionally, it has been shown that the combination of thermal oxidation and infiltration of TiO₂ by atomic layer deposition allows the manufacture of transparent GRIN optical elements with a high refractive index contrast [31]. Kruger et al. [32] used a porous silicon 1D GRIN structure infiltrated with polymer to synthesize flat micro-lens arrays. Recently, J Wang et al. has shown the fabrication of a miniature spectrometer with a PS based rugate filter using a radial interfacial potential distribution [33] On the other hand, the effect of different topographical features present on the same chip, has also been used to study the dependence of the adhesion of certain cells on the surface topography [26].

For applications such as those mentioned above, it would be very useful to be able to predict beforehand the spatially dependent properties of the resulting structures. This would allow the design and possible optimization of the desired devices. In this work, we report a simple analytical model to quantitatively analyze the spatial dependence of the current density during the electrochemical etching of Si to produce PS nanostructures with a lateral gradient. A calibration procedure may then relate the current density to the porosity and the etching rate. Thus, for a given etching current acting over for a given time, we may predict the position dependence of the index of refraction and optical thickness of the resulting inhomogeneous layer, thus allowing the prediction of the optical properties of multilayered GRIN structures. The structure of the paper is the following. In Section 2 we develop a simple analytical model to calculate the current density at any point over the GRIN structure under preparation for the case of an electrolytic cell with a simple shape. In Section 3 we provide experimental details for the synthesis of porous silicon samples with lateral refractive index gradient. Section 4 includes experimental results and their comparison with numerically evaluated parameters. Finally, we devote Section 5 to our conclusions.

2. Theory

A gradient in the optical properties of PS systems may be obtained by electrochemically attacking a Si surface with a position dependent current density $\mathbf{j}(\mathbf{r})$, as the porosity and refractive index depend on the current density, as does the etching rate and the thickness of the porous layer. Nevertheless, it is challenging to measure the *local* value of $\mathbf{j}(\mathbf{r})$ along the surface. As designing a GRIN structure with predefined parameters such as porosity and thickness at each point of a GRIN based optical device is desirable for reproducible device fabrication, we propose a simple method to compute the current density field at each point of the device. Though $\mathbf{j}(\mathbf{r})$ may be numerically calculated for any given arbitrary experimental setup, here we propose a particularly simple setup that allows an expression for the current in terms of a series that is rapidly convergent and each of whose terms is a simple analytic function. With this setup it is easy to characterize the dependence of different properties of interest on the current, and this allows the design and optimization of diverse GRIN PS devices.

We assume that our electrolytic cell has the shape of a rectangular prism (see Fig. 1) with a horizontal base of sides a and b , and filled with the electrolyte up to a height c . We assume that the walls of the cell are insulating while the bottom is completely covered with the sample, which is an electrically grounded relatively good conductor. Within the electrolyte we position an electrode which we assume is a thin conducting wire, insulated from the electrolyte but for a small tip, which we approximate as a point current source. Within the electrolyte the current density is

$$\mathbf{j} = \sigma \mathbf{E}, \quad (1)$$

with σ the conductivity, $\mathbf{E} = -\nabla\phi$ the electric field, and ϕ the electric potential. In a stationary situation $\nabla \cdot \mathbf{j} = \sigma \nabla \cdot \mathbf{E} = 0$. Thus, the potential obeys Laplace's equation within the electrolyte,

$$\nabla^2 \phi = 0. \quad (2)$$

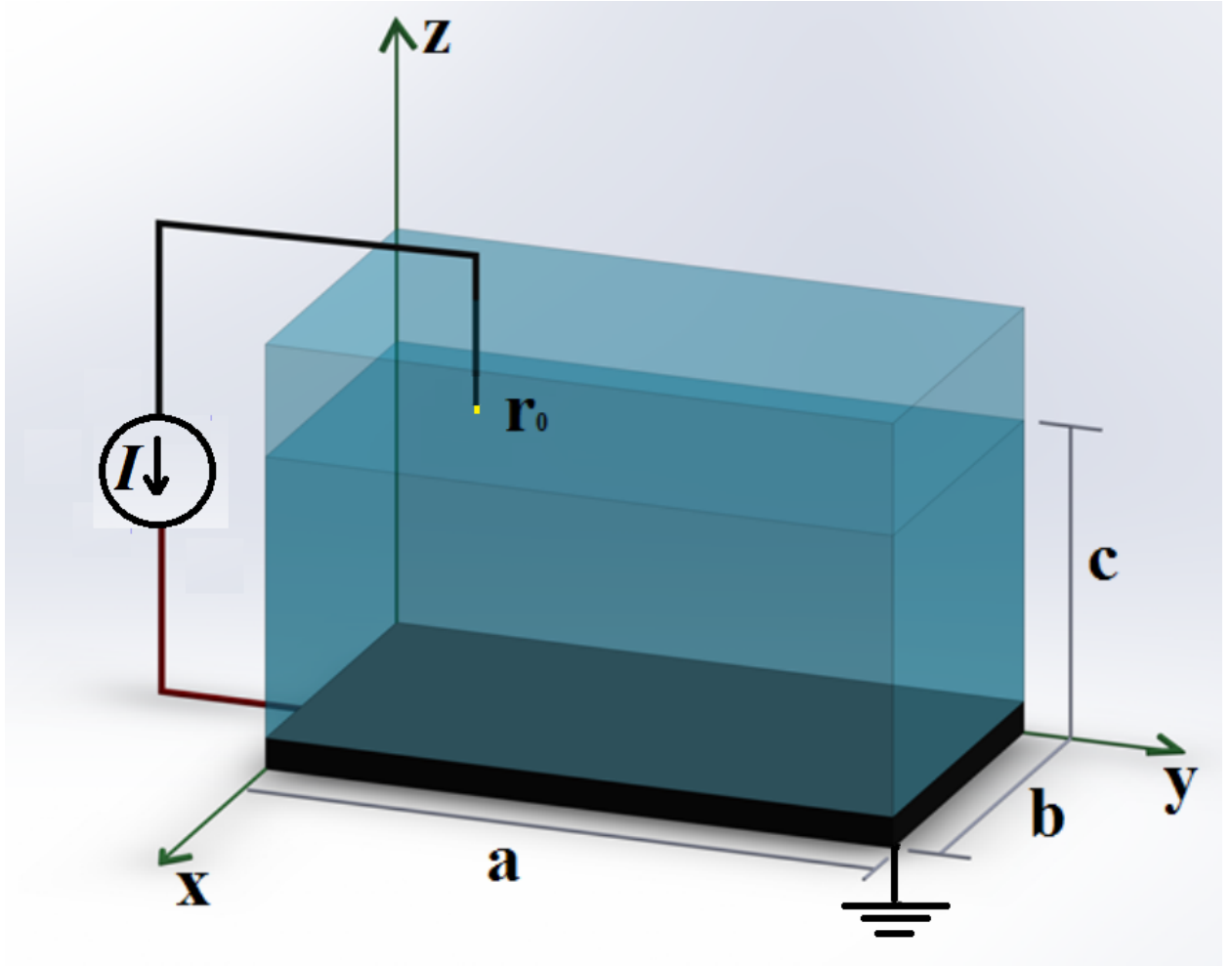


Figure 1: Prism shaped electrolytic cell with a rectangular base of sides a , b filled with electrolyte up to a height c . The walls of the cell are insulating and the bottom is completely covered by the sample, which is assumed to be a good conductor. The tip of the electrode is a thin insulated wire with just the tip uncovered and located at $\mathbf{r}_0 = (x_0, y_0, z_0)$ within the liquid. The current flows through the electrolyte from the sample to the tip.

Consider now an arbitrary closed surface S within the electrolyte that surrounds completely the tip of the electrode. Integrating \mathbf{j} over this surface we obtain

$$\int_{S'} d\mathbf{a} \cdot \mathbf{j} = -I, \quad (3)$$

where the prime on S' means we remove from the surface a very small hole through which the wire that feeds the current to the electrode gets through, and the sign is consistent with the current direction in Fig. 1. Assuming the wire is narrower than any other relevant distance in the system, we may interpret Eq. (3) as an integral over a closed surface of the current (1) within the electrolyte, ignoring the actual current within the wire. Thus

$$\int_S d\mathbf{a} \cdot \mathbf{E} = -\frac{I}{\sigma} \quad (4)$$

Using Gauss's law, we interpret this equation as a source for the potential in the form of a point charge

$$q_0 = -\frac{I}{4\pi\sigma} \quad (5)$$

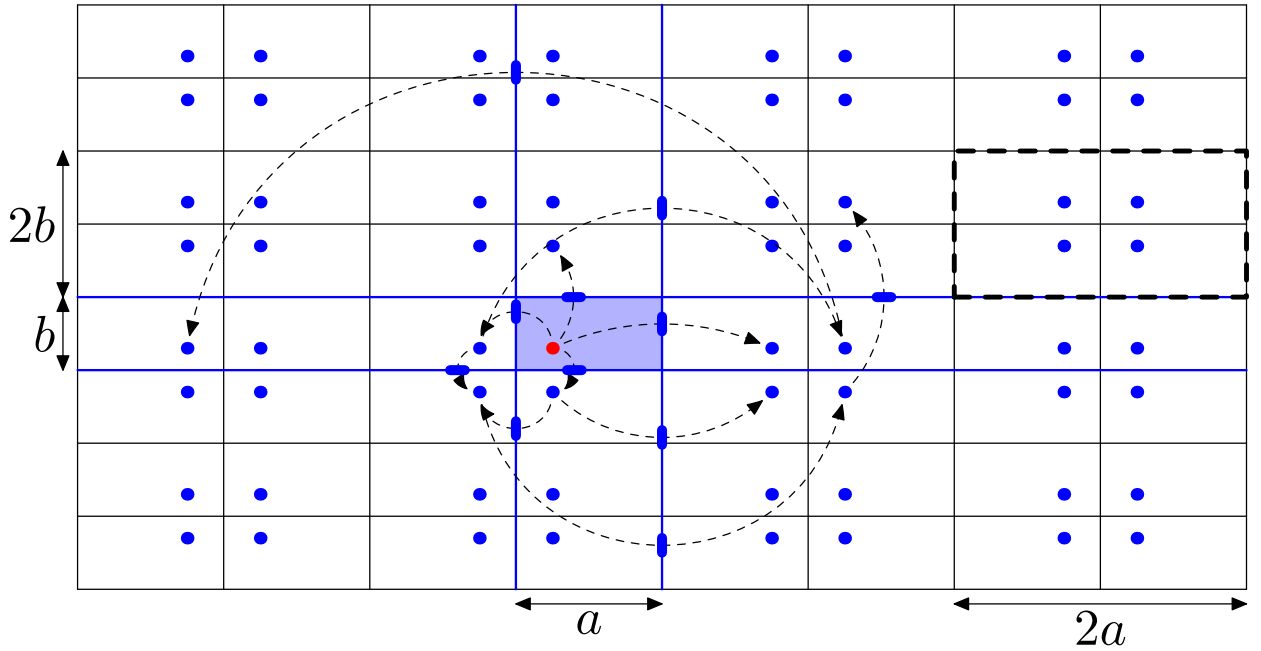


Figure 2: Top view of the $z = z_0$ plane of the fictitious system formed by reflections of the electrolytic cell (light blue) showing the charge at the tip of the electrode (red dot) and its images on the walls of the rectangular cell, the images of its images and so on (blue dots). The walls are at $x = 0, a, y = 0, b$ (blue lines). The relation of some charges and their images is indicated by dashed arrows, with a bar to indicate the corresponding reflecting wall. The system may be interpreted as a periodic lattice with a rectangular unit cell of size $2a \times 2b$, one of which is indicated by wide dashed lines, and with a basis of four equal charges q_0 at $(\pm x_0, \pm y_0, z_0)$.

at the position $\mathbf{r}_0 = (x_0, y_0, z_0)$ of the tip of the electrode. Note that q_0 would be the total charge, and it shouldn't be further screened through the permittivity of the electrolyte.

The effective conductivity of the relatively thin sample in contact with the grounded counter-electrode is large enough that we may assume its surface $z = 0$ is an equipotential. On the other hand, no current can go across the insulating walls of the cell, situated at $x = 0, x = a, y = 0$ and $y = b$, nor through the free surface of the liquid at $z = c$. Thus, the problem to solve is Poisson's equation with a point charge source

$$\nabla^2 \phi(\mathbf{r}) = -4\pi q_0 \delta^{(3)}(\mathbf{r} - \mathbf{r}_0), \quad (6)$$

with mixed boundary conditions

$$\phi(x, y, 0) = 0, \quad (7)$$

and

$$E_x(0, y, z) = E_x(a, y, z) = E_y(x, 0, z) = E_y(x, b, z) = E_z(x, y, c) = 0. \quad (8)$$

Here, $\delta^{(D)}$ is Dirac's delta function in D dimensions. This problem may be solved readily using image charge theory [34]. The potential within the electrolytic cell coincides within the region $0 \leq x \leq a, 0 \leq y \leq b, 0 \leq z \leq c$ with that within an infinite fictitious space empty but for the point charge q_0 at the tip of the electrode at \mathbf{r}_0 , and an array of its fictitious image charges situated out of the cell. They include an image on the conducting bottom of the cell, of the opposite charge $-q_0$ and situated at $(x_0, y_0, -z_0)$, to guarantee that the bottom stays at potential zero. There are further images on the four walls of the cell, of the same charge q_0 and situated at $(-x_0, y_0, z_0), (x_0, -y_0, z_0), (2a - x_0, y_0, z_0)$ and $(x_0, 2b - y_0, z_0)$ so that, taken one at a time, no current goes across the corresponding wall. Similarly, there is an image of the same charge q_0 at $(x_0, y_0, 2c - z_0)$ so that no current goes across the surface of the electrolyte. Furthermore, each image charge has to be further reflected by each of the aforementioned surfaces, yielding infinitely many new images so that Eqs. (7) and (8) hold when all charges are considered together. In Fig. 2 we illustrate the real charge and all of its images within the plane $z = z_0$. They form a periodic rectangular lattice with a unit cell of

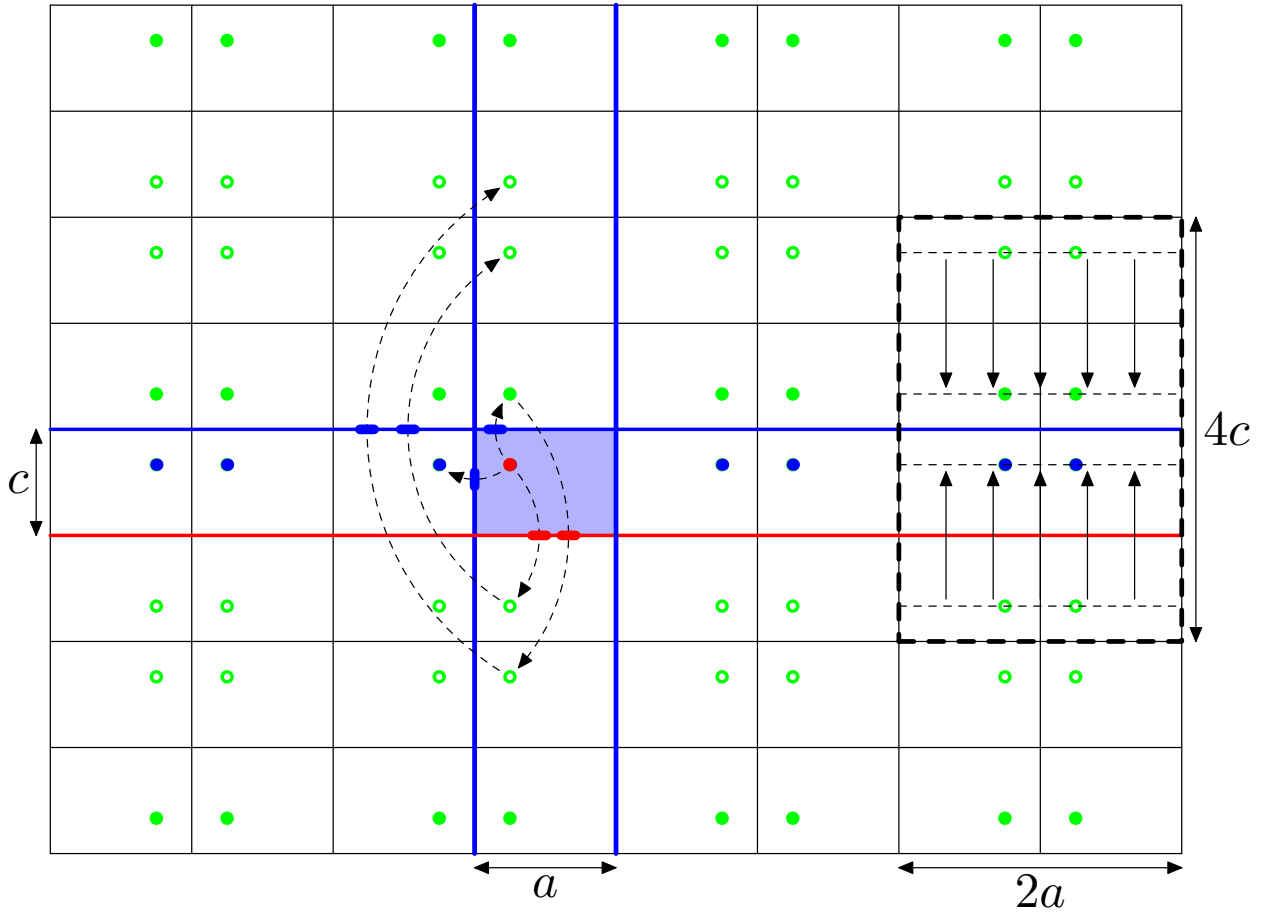


Figure 3: Side view of the $y = y_0$ plane of the fictitious system formed by reflections of the electrolytic cell (light blue) showing the charge at the tip of the electrode (red dot), its images within the plane $z = z_0$ (blue dots), and its images at the surface of the sample and the top of the electrolyte (green dots). We use solid dots to denote images with the same charge q_0 as that corresponding to the tip of the electrode, and open dots for those of opposite charge $-q_0$. The mirror planes that don't invert the charge are indicated by blue lines and the mirror plane that inverts the charge is indicated by a red line. The relation of some charges and their images is indicated by dashed arrows, with a bar to indicate the corresponding reflecting wall. The system may be interpreted as a periodic lattice with a rectangular unit cell of size $2a \times 4c$, one of which is indicated by wide dashed lines, and with a basis of four charges q_0 and another four charges $-q_0$. Within this cell, we indicate its $G = 0$ contribution to the electric field (solid arrows, see text).

size $2a \times 2b$ and with a basis of four equal charges q_0 situated at the positions \mathbf{r}_0 , $\mathbf{r}_1 = (-x_0, y_0, z_0)$, $\mathbf{r}_2 = (x_0, -y_0, z_0)$ and $\mathbf{r}_3 = (-x_0, -y_0, z_0)$. In Fig. 3 we show a lateral view of the image charges within the plane $y = y_0$. Each plane of charges upon reflection on the surface of the sample at the bottom of the cell yields a plane of image charges of the opposite sign, while each reflection on the surface of the liquid yields a plane of charges of the same sign. The side view may be interpreted as a periodic rectangular lattice with a unit cell of size $2a \times 4c$ containing a basis of eight point charges, four positive and four negative. A projection onto the yz plane would similarly yield a rectangular lattice with a $2b \times 4c$ unit cell. Putting everything together, the problem is that of solving Poisson's equation within an orthorhombic lattice of size $2a \times 2b \times 4c$ with a basis of 16 point charges of charge $\pm q_0$ arranged in positive and negative planes.

The electrostatic potential produced by an infinite array of charges expressed as a sum in real space of Coulomb terms has ill convergence properties. The potential can be obtained using the Ewald summation technique [35–41], which yields two rapidly converging series, one in real space and another one in reciprocal space. Nevertheless, as we need the potential and the field to obtain the current density on the surface of the sample on which no real nor image

charges lie, we may perform a somewhat simpler plane-wise summation, where we first obtain the potential and field produced by a simple periodic lattice of charges using a fast convergent sum over the two dimensional (2D) reciprocal vectors [42–46], then sum over the charges that form the basis of the 2D *crystal* plane, and finally sum over all the planes.

We consider first a system made of identical *unit* charges occupying the positions \mathbf{R} of a 2D Bravais lattice $\{\mathbf{R}\}$, which we will take as a rectangular lattice with lattice parameters $2a$ and $2b$, and lying, for the time being, at the $z = 0$ plane. The potential ϕ it produces obeys

$$\nabla^2 \phi(\mathbf{r}) = -4\pi \sum_{\mathbf{R}} \delta^{(2)}(\mathbf{r}_{\parallel} - \mathbf{R}) \delta^{(1)}(z) = -\frac{4\pi}{A} \sum_{\mathbf{G}} e^{i\mathbf{G}\cdot\mathbf{r}_{\parallel}} \delta^{(1)}(z), \quad (9)$$

where \mathbf{r}_{\parallel} is the projection of the observation position $\mathbf{r} = (x, y, z)$ onto the xy plane, $\{\mathbf{G}\}$ is the 2D reciprocal lattice defined through $e^{i\mathbf{G}\cdot\mathbf{R}} = 1$ for all \mathbf{R} and \mathbf{G} , $A = 4ab$ is the area of the unit cell and we used the Fourier representation of the 2D periodically repeated delta function. We introduce a 2D Fourier representation for the potential

$$\phi(\mathbf{r}) = \sum_{\mathbf{G}} \phi_{\mathbf{G}}(z) e^{i\mathbf{G}\cdot\mathbf{r}_{\parallel}} \quad (10)$$

where $\phi_{\mathbf{G}}(z)$ is the 2D Fourier coefficient of the potential at the height z . Substitution in Eq. (9) yields the ordinary differential equation

$$\frac{d^2}{dz^2} \phi_{\mathbf{G}}(z) - G^2 \phi_{\mathbf{G}}(z) = -\frac{4\pi}{A} \delta^{(1)}(z), \quad (11)$$

for each coefficient, an homogeneous equation for $z \neq 0$ which may be trivially solved. After applying boundary conditions at $z = 0$ and regularity conditions at infinity (for $G \neq 0$), we obtain

$$\phi_{\mathbf{G}}(z) = \begin{cases} -\frac{2\pi}{A} |z| & \text{if } G = 0, \\ \frac{2\pi}{AG} e^{-G|z|} & \text{if } G \neq 0. \end{cases} \quad (12)$$

The case $G = 0$ corresponds to the potential produced by a uniformly charged plane, while the case $G \neq 0$ is the potential produced by a sinusoidal charge density on a plane, given by the symmetric solution that decays exponentially as we get away, upwards or downwards, from the source plane. Substituting into Eq. (10) yields

$$\phi(\mathbf{r}) = -\frac{2\pi}{A} |z| + \sum'_{\mathbf{G}} \frac{2\pi}{AG} e^{-G|z|} e^{i\mathbf{G}\cdot\mathbf{r}_{\parallel}}, \quad (13)$$

where the prime indicates that the term $G = 0$ should be omitted from the sum.

We consider now the basis of our 2D lattice, with equal charges at the four positions $(\pm x_0, \pm y_0, 0)$. Each of the corresponding four sub-lattices produces a potential as that in Eq. (13) but shifted by the corresponding basis vector, yielding

$$\phi(\mathbf{r}) = -\frac{8\pi}{A} |z| + \sum'_{\mathbf{G}} \frac{8\pi}{AG} e^{-G|z|} \cos(G_x x_0) \cos(G_y y_0) e^{i\mathbf{G}\cdot\mathbf{r}_{\parallel}}. \quad (14)$$

Finally, we shift the origin of Eq. (14) vertically to each of the planes shown in Fig. 3 and multiply by the corresponding charge q_0 or $-q_0$ to obtain the contribution to the total potential. The charge q_0 corresponds to the planes with heights of the form $z_0 + 4nc$ and $-z_0 + (4n + 2)c$, with $n = \dots - 2, -1, 0, 1, 2 \dots$ an arbitrary integer, while the charge $-q_0$ corresponds to the planes with heights $z_0 + (4n + 2)c$ and $-z_0 + 4(n + 1)c$.

We concentrate our attention only on the region $0 \leq z < z_0$ above the sample but below the electrode. From Fig. 3 we see that the $G = 0$ field has contributions only from the charges at z_0 and their images at $-z_0$, and that this contribution is like that of a parallel plate capacitor $E_{0z} = -4\pi q_0 / ab = -16\pi q_0 / A$, which corresponds to the potential $\phi_0 = 16\pi q_0 z / A$. Other pairs of contiguous planes with opposite charges contribute to the field elsewhere.

The contributions to the potential from the $G \neq 0$ terms are simple geometric series that may be summed over n analytically and yield the total potential

$$\phi(\mathbf{r}) = \frac{16\pi q_0}{A} \left(z + \sum'_G \frac{2 \sinh Gc}{G \sinh 2Gc} \cosh G(c - z_0) \cos G_x x_0 \cos G_y y_0 \times \sinh Gz e^{i\mathbf{G} \cdot \mathbf{r}_{\parallel}} \right). \quad (15)$$

Notice that the terms of the sum above converge exponentially to zero as G increases for any z such that $0 \leq z < z_0 \leq c$, and thus the sum is convergent. The divergence in the limit $z \rightarrow z_0$ corresponds to the singularity of the potential at the position of a point charge, and it is not worrisome, as we are interested in the field close to bottom $z = 0$ of the cell.

The current density normal to the surface may now be obtained as $j_{\perp} = -\sigma \partial \phi / \partial z$,

$$j_{\perp}(\mathbf{r}) = \frac{I}{ab} \left(1 + \sum'_G \frac{2 \sinh Gc}{\sinh 2Gc} \cosh G(c - z_0) \cos G_x x_0 \cos G_y y_0 \times \cosh Gz e^{i\mathbf{G} \cdot \mathbf{r}_{\parallel}} \right). \quad (16)$$

Eq. (16) is a very rapidly convergent expression that allows, in particular, to calculate the current $j_{\perp}(x, y, 0)$ that attacks the substrate to produce the PS sample. As expected, the current at the surface $z = 0$ of the sample becomes more homogeneous as the distance z_0 to the tip of the electrode and the height of the electrolyte $c > z_0$ increase, as each term in the sum decays approximately exponentially with increasing z_0 . Integrating over the surface of the sample we verify

$$\int_0^a dx \int_0^b dy j_{\perp}(\mathbf{r}) = I, \quad (17)$$

as the contributions of opposite non-null reciprocal vectors cancel out: as expected, all the charges that leave the sample find their way to the cathode across the electrolyte.

Using Eq. (16) we can correlate the local current density at the sample as it is prepared with its geometric, structural and optical properties.

3. Procedures

In Fig. 4 we show a schematic representation of our experimental setup to manufacture GRIN PS structures. As discussed above, we fabricated an electrolytic cell with the shape of a rectangular prism on the bottom of which we place a Si wafer which makes electrical contact to a brass plate which together make the anode. The cathode consists of a platinum wire insulated except for a small region at its tip, which we take as a point current drain. We also show a schematic drawing of the expected GRIN PS structures, with a gradient in the porosity, and in the thickness, density and depth of the resulting pores.

3.1. Fabrication of PS GRIN Single Layers

Single layer PS structures were fabricated through electrochemical anodization of (100) oriented p -type crystalline Si wafer (resistivity 0.002 - 0.005 Ω cm), under galvanostatic conditions. The process was performed at room temperature with an electrolytic mixture of aqueous hydrofluoric acid (HF) (concentration 48% wt), glycerol (purity 99.8 % wt) and ethanol (purity 99.9% wt) in a 3:7:1 volume ratio. After the anodizing process, the samples were rinsed with ethanol (purity: 99.9 % wt). The electrolytic cell had the shape of a rectangular prism as shown in Fig. 4, with a base of sides $a = 2.01$ cm and $b = 1.48$ cm, with an uncovered sample area of about 3 cm². The height of the liquid was set at $c = 1$ cm. The cathode was a platinum wire with a diameter of 0.41 mm insulated with Teflon tape, with an uncovered tip located at $\mathbf{r}_0 = (x_0, y_0, z_0) = (0.2$ cm, 0.74 cm, 0.9 cm). We manufactured three samples S_1 , S_2 and S_3 by applying a current $I_1 = 5$ mA, $I_2 = 10$ mA and $I_3 = 20$ mA, respectively, during a time of $t = 250$ s.

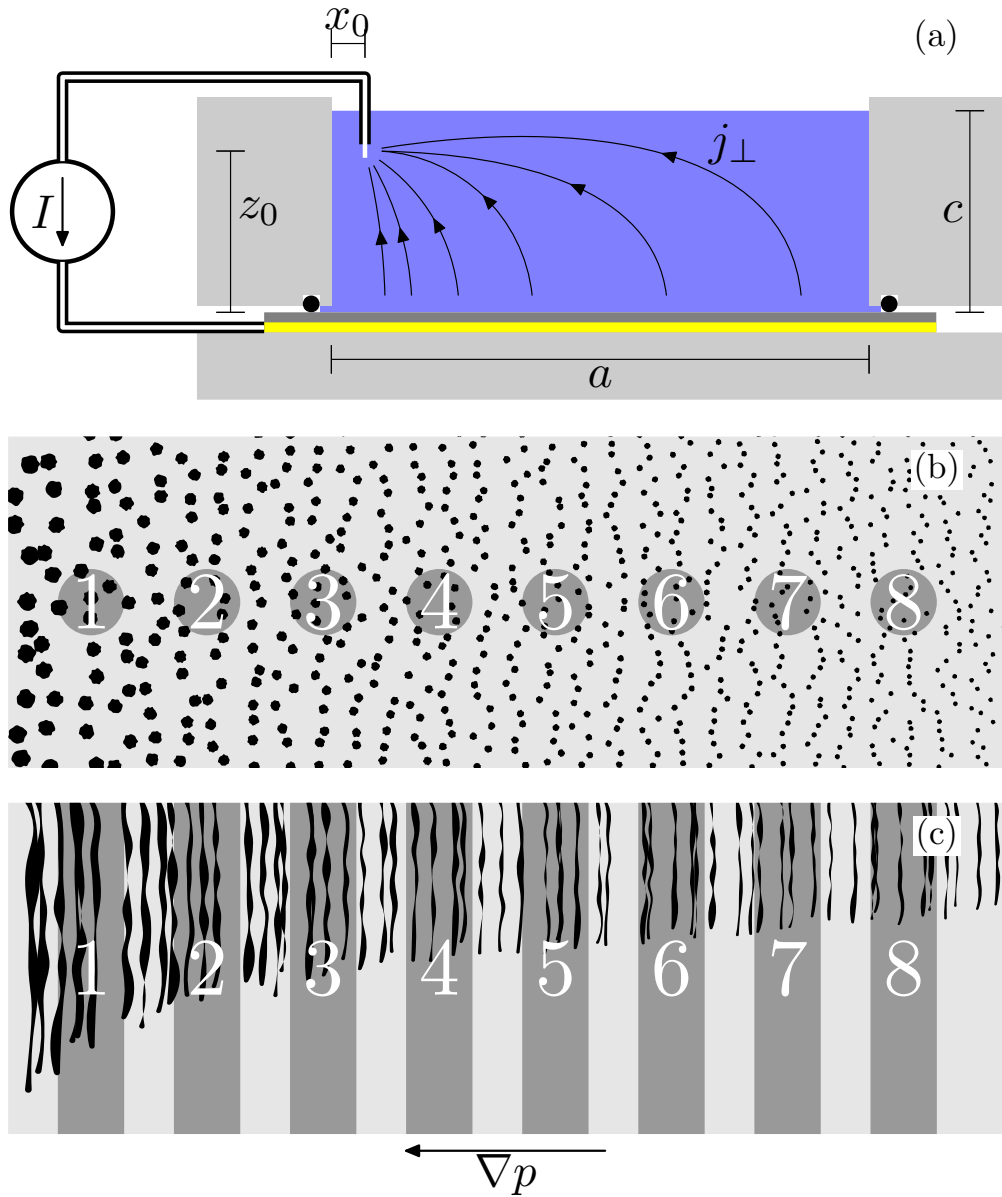


Figure 4: (a): Schematic experimental set-up for the fabrication of GRIN PS structures. We show a side view of the electrochemical cell with the shape of a rectangular prism. We indicate the Si wafer (dark gray), the Teflon cell (light gray), the sealing o-ring (black circles), the insulated feeding cable (white lines within black lines), the uncovered platinum tip (white) within the electrolyte (blue), the electrical contact below the sample (yellow) and the controlled current source. We indicate some geometrical parameters of the arrangement x_0 , z_0 , a and c and a few schematic current flux lines. (b) and (c): Top and side schematic views of expected resulting sample illustrating eight regions 1 ... 8 of decreasing porosity and thickness, illustrating the changes in pore radii, length, and density and the porosity gradient.

3.2. Reflectance Measurement

We measured the absolute reflectance at different positions over our samples using Universal reflectance accessory equipped *Perkin Elmer Lambda 950* ultraviolet-visible-near infrared (UV-Vis-NIR) spectro-photometer, with a rectangular spot size of $0.7\text{mm} \times 2.0\text{mm}$, a slit width of 0.6mm in a wavelength range from 300nm to 1400nm .

For interpretation of the data we used the standard formula [47] for the reflectance of a three media system: an air

environment (0), the PS film (1) and the crystalline Si (c-Si) substrate (2),

$$R = \left| \frac{r_{01} r_{12} e^{2i\psi}}{1 + r_{01} r_{12} e^{2i\psi}} \right|^2 \quad (18)$$

where r_{01} and r_{12} are the Fresnel reflectance coefficients of the air/PS and PS/c-Si interfaces [48] and $\psi = k_1^\perp d$, where k_1^\perp is the component of the wave-vector perpendicular to the surface within the porous layer of thickness d . The reflectance depends on the thickness of the film and on the index of refraction $n_1 = n_{\text{PS}}$ of the porous layer, which we relate to the porosity through Bruggeman's effective medium theory [49],

$$p \frac{1 - \epsilon_1}{1 + \epsilon_1} + (1 - p) \frac{\epsilon_2 - \epsilon_1}{\epsilon_2 + \epsilon_1} = 0, \quad (19)$$

where $\epsilon_2 = \epsilon_{\text{Si}}$ is the dielectric function of the c-Si substrate and $\epsilon_1 = n_{\text{PS}}^2$ is the dielectric function of the PS layer. We fitted the reflectance spectra using the porosity p and the thickness d and a scale calibration factor s as fitting parameters, and thus, we obtained the porosity p and the etching rate $v = d/t$ for different values of the local current density j_\perp expected at several positions on different samples.

3.3. Morphological studies

The morphology of the etched porous layers (plan-view and cross-sectional) was observed with a *Hitachi SU1510* scanning electron microscope (SEM).

4. Results and Discussion

4.1. Current Density

In Fig. 5 we show the normalized current density $j_\perp(x, y, 0)/I$ calculated through Eq. (16) at the surface of the sample for our cell, as shown in Figs. 1 and 4 and described in Sect. 3.1). For these parameters we obtained a large range of values for $j_\perp/I \sim 0.11 - .72 \text{ cm}^{-2}$ that vary mostly along the x direction. Of course, this would differ for cells with different aspect ratios and for different positions of the electrode.

4.2. Samples

In Fig. 6 we show a photograph of one of our samples, S_3 , prepared as described in Sec. 3.1, with the same conditions as those corresponding to Fig. 5 applying a current $I_3 = 20 \text{ mA}$ during a time $t = 250 \text{ s}$. We notice a series of visible interference fringes that get wider as we move towards the right end of the sample, consistent with an inhomogeneous film that gets thinner towards the right, and qualitatively consistent with Fig. 5 that shows a current density that decays towards the right. Equal color lines seem to correspond to iso-current lines of Fig. 6, except very close to the walls of the cell, where the film rapidly becomes very narrow. The reason is that there is a small region below the cell walls where the electrolyte penetrates up to the sealing o-ring (see upper panel of Fig. 4) and towards which the current leaks from the neighborhood of the wall. The width of this region is $w = 0.14 \text{ cm}$. Thus, we may expect our formula (16) to *fail* within that region and close to the border, at distances of the order of the radius of the cross-section of the o-ring, about a millimeter. The figure shows eight positions $x'_n = 0.2 \text{ cm}, 0.4 \text{ cm}, \dots, 1.6 \text{ cm}$ on which we measured the near normal incidence reflection spectra of the sample. Here, we defined $x'_n = x_n + w$ as the distance to the edge of the etched sample, which corresponds to the position of the sealing o-ring, whereas x_n is the corresponding distance to the wall of the cell.

From Eq. (16) we evaluate the normalized current density j_\perp/I expected at the positions n indicated in Fig. 6. We included an estimated uncertainty $\Delta x_n = \Delta x$ in the distances x_n to the wall of the cell, and the corresponding (asymmetrical) uncertainty in the computed current density. This uncertainty arises from the uncontrolled deformation of the o-ring as it is pressed against the wafer to seal in the electrolyte, so that its distance $x'_n - x_n \approx 0.14 \text{ cm} \pm \Delta x$ to the wall of the cell is not well determined. We estimate Δx as the radius of the o-ring (Table 1).

In Fig. 7 we show some SEM images of the sample S_3 , including top views and lateral views taken after the optical characterization was completed and the sample was cut along its center-line (see Sec. 4.3) from three regions around the left side, the center, and the right side of the sample shown in Fig. 6. We confirm that as we move away from the electrode, the pore size and pore density diminish (panels (a) to (c) of Fig. 7) and the sample becomes much thinner

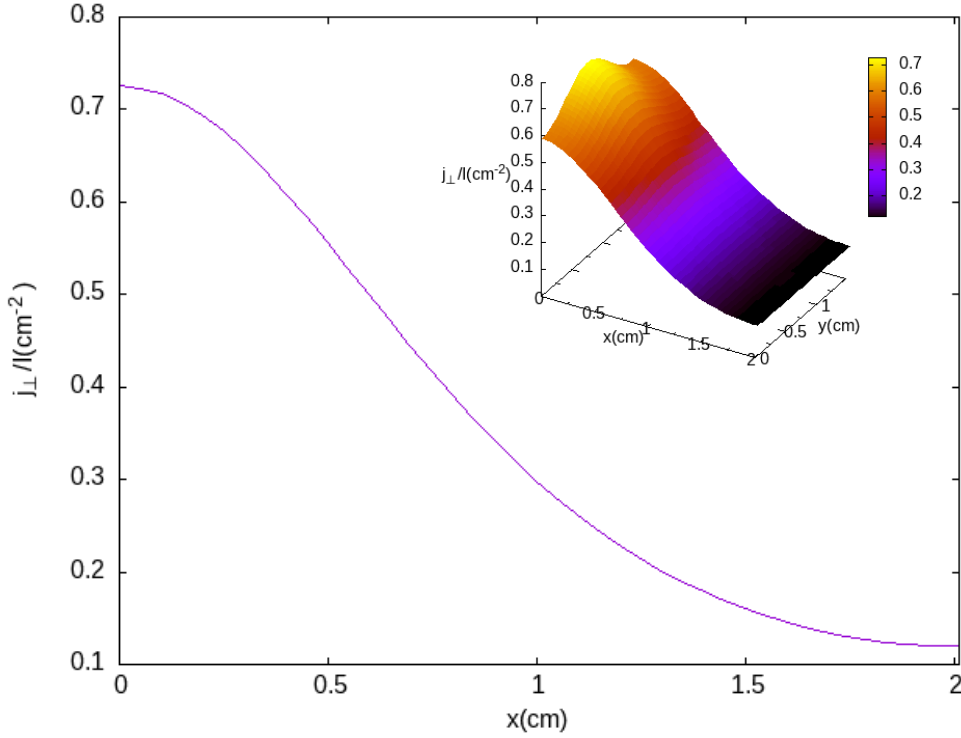


Figure 5: Normalized current density $j_{\perp}(x, y, 0)/I$ for a system as in Figs. 1 and 4 for a cell of length $a = 2.01$ cm and width $b = 1.48$ cm, with the surface of the electrolyte at a height $c = 1.0$ cm, with a point-like electrode at $\mathbf{r}_0 = (0.2 \text{ cm}, 0.74 \text{ cm}, 0.9 \text{ cm})$, calculated through Eq. (16) along the center line $y = 0.74$ cm. Inset: current over the whole surface.

x'_n (cm) from edge	x_n (cm) from wall	j_{\perp}/I (cm ⁻²)
0.2	0.06 ± 0.05	$0.722^{+0.003}_{-0.007}$
0.4	0.26 ± 0.05	$0.672^{+0.018}_{-0.021}$
0.6	0.46 ± 0.05	$0.577^{+0.027}_{-0.028}$
0.8	0.66 ± 0.05	$0.464^{+0.028}_{-0.028}$
1.0	0.86 ± 0.05	$0.360^{+0.025}_{-0.023}$
1.2	1.06 ± 0.05	$0.275^{+0.019}_{-0.018}$
1.4	1.26 ± 0.05	$0.211^{+0.014}_{-0.013}$
1.6	1.46 ± 0.05	$0.167^{+0.010}_{-0.009}$

Table 1
Normalized current density j_{\perp}/I expected at different positions x'_n .

(panels (d) to (f)). We remark that these micrographs were taken at three positions that were not chosen to correspond to the eight locations at which we measured the optical spectra. Thus, we didn't use SEM measurements for the quantitative determination of neither the thickness nor the porosity; they were used for the qualitative verification of the expected (Fig. 4) and obtained (Table 2) results. Actually, one of our goals is to show that relatively inexpensive reflectance measurements might be enough to characterize both the porosity and etching rate variations along the sample.

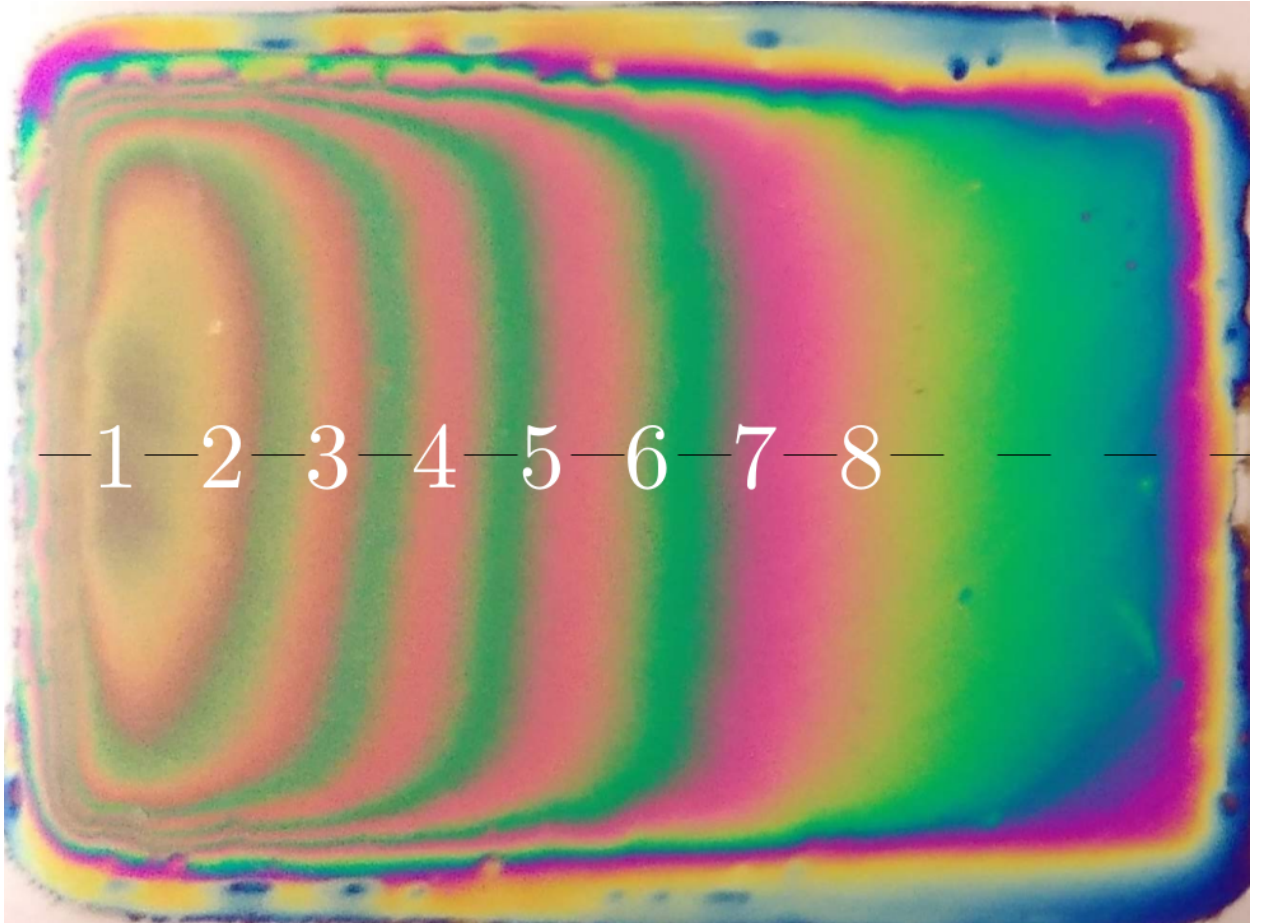


Figure 6: Photograph of sample S_3 prepared as described in Sec. 3.1 using the same parameters as in Fig. 5 with a current $I_3 = 20\text{mA}$, during a time $t = 250\text{s}$. We indicate the center-line with a dashed line and eight regions x_i ($i = 1, 2, \dots, 8$) centered at positions, $x'_1 = 0.2\text{cm}$, $x'_2 = 0.4\text{cm}$, $x'_3 = 0.6\text{cm}$, $x'_4 = 0.8\text{cm}$, $x'_5 = 1\text{cm}$, $x'_6 = 1.2\text{cm}$, $x'_7 = 1.4\text{cm}$, $x'_8 = 1.6\text{cm}$, with $y_n = 0.74\text{cm}$ on which we measured reflectance spectra. Here, $x'_n = x_n + 0.14\text{cm}$ is the position from the left side sealing o-ring.

4.3. Reflectance

We measured the reflectance spectra at the positions indicated in Fig. 6 on our three samples S_1 , S_2 , and S_3 , prepared using the same procedure (Sec. 3.1) but applying different currents $I_1 = 5\text{mA}$, $I_2 = 10\text{mA}$, and $I_3 = 20\text{mA}$. The results are shown in Figs. 8, 9, and 10. We fitted the reflectance measurements using Eqs. (18) and (19) using the local porosity p , and the thickness of the film d as adjustable parameters. To that end we used the `migrad` routine of the `Minuit` minimization software. From the thickness we obtained the etching rate $v = d/t$ at each position. Notice that the fits are reasonably good. The contrast of the reflectance in the experiment is somewhat smaller than in our fitted curves. We believe this is due to the finite width $0.7\text{mm} \times 2.0\text{mm}$ of the illuminating beam of our spectrometer. Thus, as our GRIN sample is not macroscopically homogeneous and its properties have a gradient, the experimental results have contributions from regions with slightly different porosities and thicknesses, partially averaging out the interference maxima and minima. We expect microscopic inhomogeneities such as interface roughness might also reduce the contrast through scattering and its corresponding apparent dissipation [50]. The loss of contrast is most notable for the thicker regions towards the left side of Fig. 6 and for smaller wavelengths.

The results obtained from the reflectance fits are summarized in table 2. The uncertainties in the fitted parameters p , d , and v were chosen as those that increase the sum of squared errors by 10% with respect to its minimum value.

From the data in Table 2 we can plot the fitted porosity vs. the calculated density current j_{\perp} , as shown for our three samples in Fig. 11. Notice that for each sample the data points lie around straight lines, except for one outlier point in

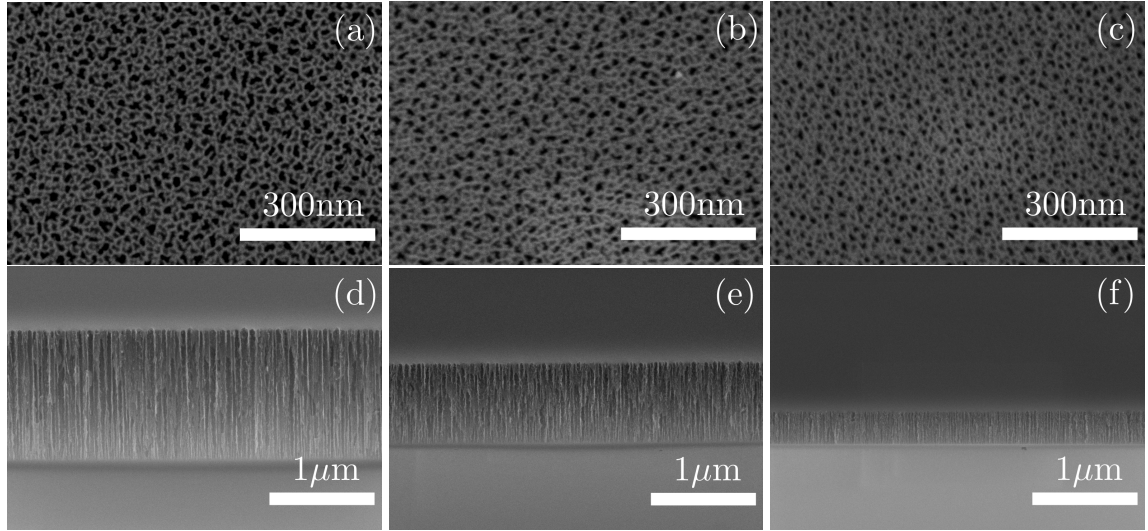


Figure 7: Top ((a), (b), and (c)) and lateral ((d), (e), and (f)) SEM micrographs of the sample S_3 taken from a region corresponding to the left side ((a) and (d)), center ((b) and (e)), and right side ((c) and (f)) along the center-line shown in Fig. 6.

each corresponding to position x'_1 . As discussed in Sec. 4.2, those points were very close to a wall of the electrolytic cell, so they were affected by leakage currents towards the underside of the wall. For this reason, we exclude those points from the following analysis. We made a linear fit of the form $p = mj_{\perp} + b$ obtaining

$$p \approx (0.0122 \pm 0.001) \frac{\text{cm}^2}{\text{mA}} j_{\perp} + (0.551 \pm .005). \quad (20)$$

Though the fit is reasonably good, it is noticeable that most of the data from sample S_2 lie to the left of the fitted line while most of the data from the other samples lie to the right. This discrepancy may be due to the uncertainty in the positions x_n (see Table 1) due to the ill defined distance from the edge of the sample (which roughly corresponds to the position of the o-ring) to the edge of the cell. A deformation of the o-ring when the cell is pressed against the wafer would be equivalent to a rigid shift of the sample, i.e., to adding a constant to all the positions x_n . Thus it is likely that the sign and magnitude of that uncontrolled constant displacement changes among samples.

Similarly, we can plot the fitted etching rate vs. the calculated density current, as shown for our three samples in Fig. 12. As for the porosity, excluding the points in the immediate proximity of the wall of the cell, the remaining points lie roughly on straight lines for each sample, and they may all be approximated by a linear fit to all the data, from which we get

$$v \approx (0.312 \pm 0.017) \frac{\text{cm}^2}{\text{mA}} \frac{\text{nm}}{\text{s}} j_{\perp} + (0.44 \pm 0.09) \frac{\text{nm}}{\text{s}}. \quad (21)$$

Similarly to Fig. 11, most data from sample S_2 lies to the left of the fitted line and most of the data from S_1 and S_3 lie to the right, which could be similarly explained and corrected. These corrections are different for layers grown on different samples, but for a multilayered system, produced by modulating the current I in time, a single correction ought to be enough for all the layers.

Using Eqs. (18)-(21) we can calculate the reflectance spectra for any desired current density j_{\perp} and etching time. This is illustrated in Fig. 13 for the parameters that correspond to our samples. On the right hand side of the figure we display a quilt made by patching together the experimental reflectance data corresponding to Figs. 8- 10, ordered according to the corresponding current density as presented in Table 2. Nevertheless, for the reasons mentioned above, we eliminated the data corresponding to position x'_1 on all samples. Furthermore, as discussed above and for visualization purposes we applied small rigid translations to the samples along the x direction, thereby modifying j_{\perp} , before patching together the reflectance spectra. Notice that the experimental results may be grouped along bright and dark bands that correspond closely to those expected theoretically, though the experimental bands are somewhat shifted, especially for low current densities, and their minima are not as low.

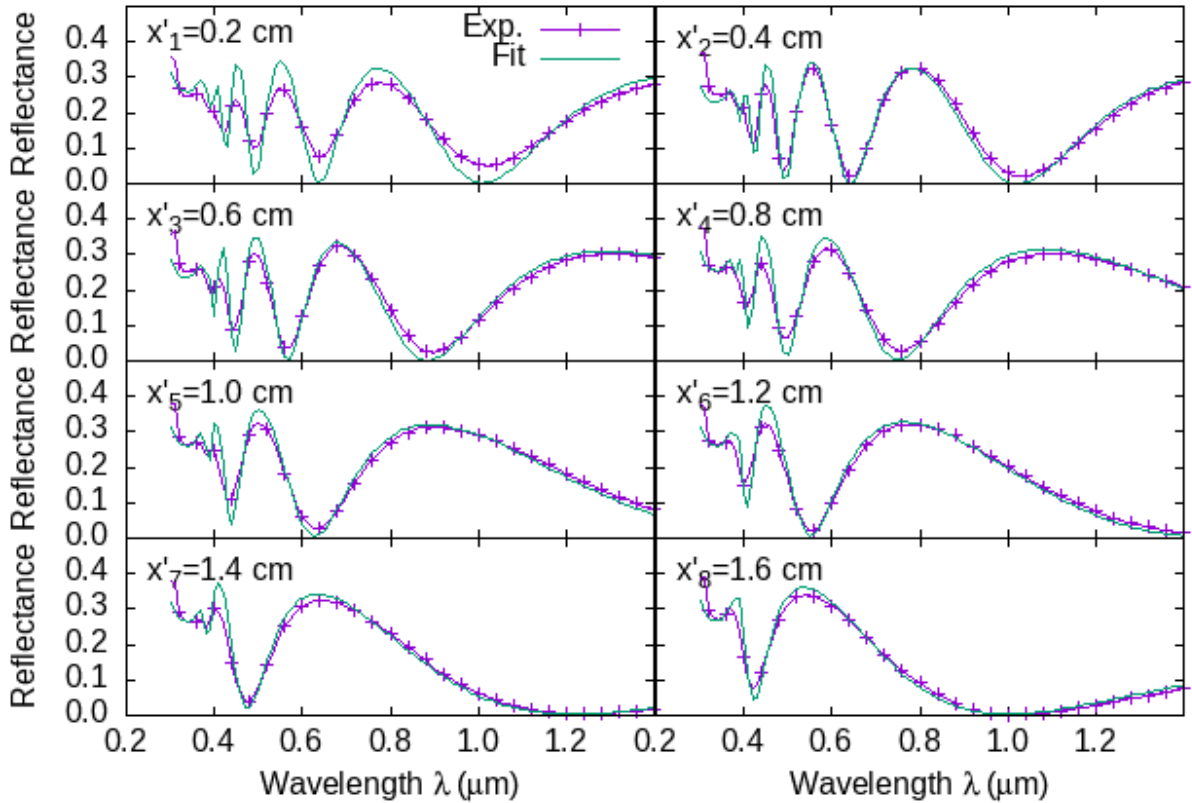


Figure 8: Reflectance spectra at different positions ($x'_n = 0.2 - 1.6$ cm, $y = 0.74$ cm) on sample S_1 ($I_1 = 5$ mA). We show experimental results and results fitted through equations (18) and (19)

The theoretical reflectance could as well be calculated using Eqs. (19)-(21) and a transfer matrix approach for more complicated structures, in which the current I is modulated in time, allowing the design and analysis of non-trivial multilayered GRIN PS structures.

5. Conclusions

By choosing a simple geometry for our electrochemical cell, namely, a rectangular prism, and employing a point-like electrode, we were able to derive an expression for the calculation of the electric current density along the surface of a Si sample. The expression was obtained by using image charge theory and a plane-wise summation of Coulomb potentials in 2D reciprocal space, and it is made up of a rapidly converging sum of analytical terms, just a few of which need be kept. This allows the characterization of the porosity of a PS layer and the etching rate for different values of the etching current density by making optical measurements on several positions of just a few samples. We illustrated the procedure with three samples on each of which we measured reflectance spectra at eight different positions. Through an optimization procedure, we fitted the porosity and etching rates corresponding to each current density. We used these data to obtain calibration curves that allow the approximate prediction of the properties of porous Si samples prepared with a current density that spans a range of more than one order of magnitude. The small discrepancies we found between our samples and the fit are probably due to our unfortunate choice of reference point for measuring positions, as we used as reference the ill defined edge of the sample, while the important reference for our calculation is the edge of the wall of the electrolytic cell. Nevertheless, these discrepancies are reduced through a rigid shift of the

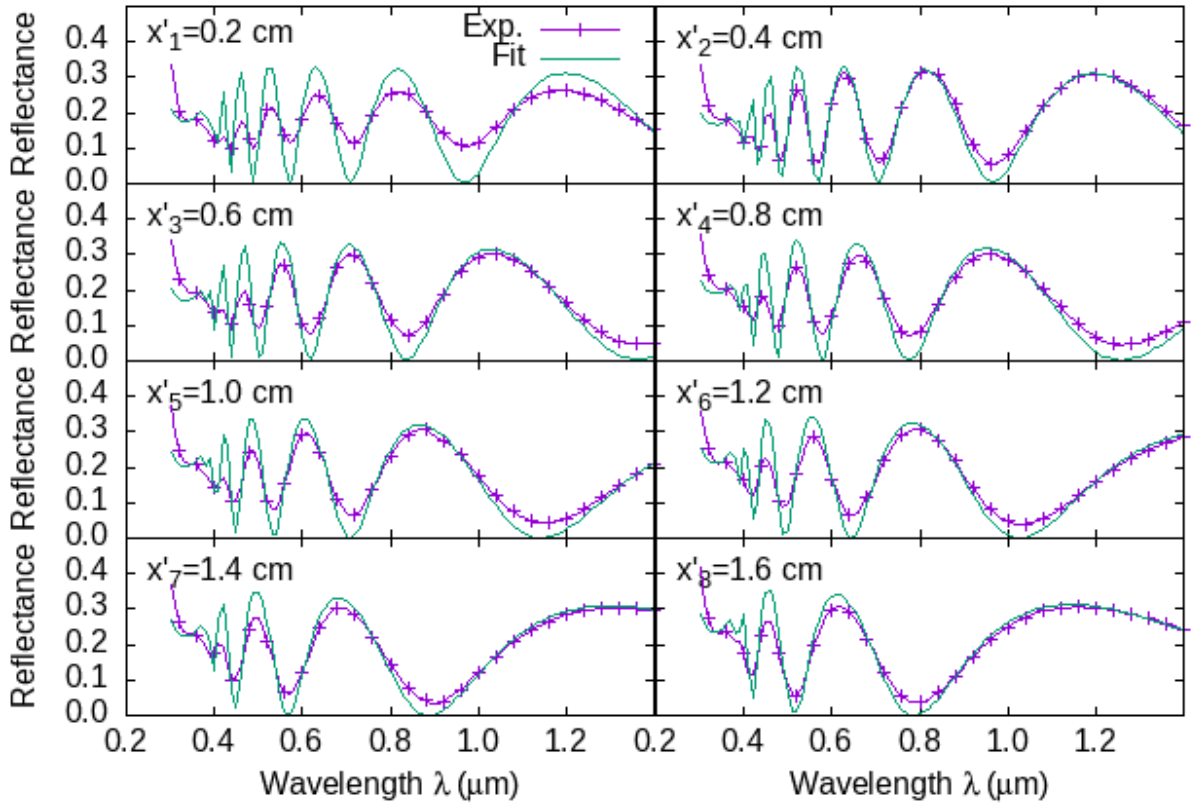


Figure 9: Reflectance spectra at different positions ($x'_n = 0.2 - 1.6$ cm, $y = 0.74$ cm) on sample S_2 ($I_1 = 10$ mA). We show experimental results and results fitted through equations (18) and (19)

coordinates x_n used in the analysis. Our calibration curves can be used to design and calculate the optical properties of other systems prepared under similar conditions, such as multilayered GRIN systems from which photonic crystals, micro-cavities and sensors with position-dependent properties. This is the subject of ongoing work. As the etching rate for the formation of porous silicon and the resulting porosity are very sensitive to the growth conditions and to the properties of the substrate, such as its doping, there are no universal calibration curves. Thus, it is useful to have a procedure that from just one or a few samples can produce calibration curves that may be employed for other samples grown under similar conditions.

Acknowledgments

CAOD is grateful for a scholarship from CONACyT and to V. Castillo-Gallardo and L.E. Puente Díaz for useful discussions. VA acknowledges support from CONACyT Basic Sciences project A-S1 30393 and from PRODEP, and is grateful to ICF where she spent a sabbatical. WLM acknowledges the support of DGAPA-UNAM under grant IN111119.

CRedit authorship contribution statement

C. A. Ospina-Delacruz: Investigation; Software; Writing - original draft. **V. Agarwal:** Funding acquisition; Investigation; Supervision; Software; Writing - review & editing. **W. L. Mochán:** Conceptualization; Funding acquisition; Investigation; Methodology; Supervision; Writing - review & editing.

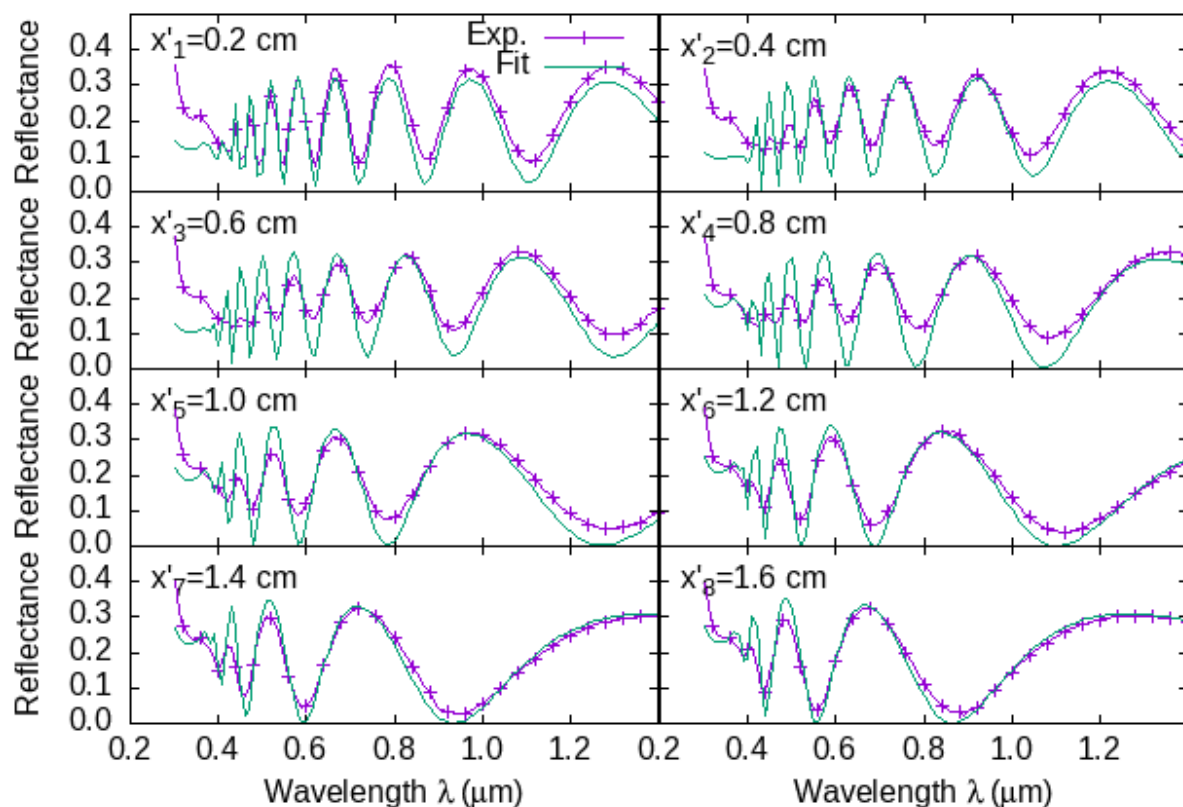


Figure 10: Reflectance spectra at different positions ($x'_n = 0.2 - 1.6$ cm, $y = 0.74$ cm) on sample S_3 ($I_3 = 20$ mA) (Fig. 6). We show experimental results and results fitted through equations (18) and (19)

References

- [1] Barbara K Pierscionek and Justyn W Regini. The gradient index lens of the eye: An opto-biological synchrony. *Progress in retinal and eye research*, 31(4):332–349, 2012.
- [2] Shumeng Bai, Xueliang Zhang, Xueli Lv, Mengya Zhang, Xiaowei Huang, Yu Shi, Chunhua Lu, Jibin Song, and Huanghao Yang. Bioinspired mineral–organic bone adhesives for stable fracture fixation and accelerated bone regeneration. *Advanced Functional Materials*, 30(5):1908381, 2020.
- [3] Wilhelm F Maier, Klaus Stoewe, and Simone Sieg. Combinatorial and high-throughput materials science. *Angewandte chemie international edition*, 46(32):6016–6067, 2007.
- [4] Shrisudersan Jayaraman and Andrew C Hillier. Construction and reactivity screening of a surface composition gradient for combinatorial discovery of electro-oxidation catalysts. *Journal of combinatorial chemistry*, 6(1):27–31, 2004.
- [5] Radislav A Potyrailo and Vladimir M Mirsky. Combinatorial and high-throughput development of sensing materials: The first 10 years. *Chemical Reviews*, 108(2):770–813, 2008.
- [6] Stephen E Fosdick, John A Crooks, Byoung-Yong Chang, and Richard M Crooks. Two-dimensional bipolar electrochemistry. *Journal of the American Chemical Society*, 132(27):9226–9227, 2010.
- [7] Rajakumari Ramaswamy and Curtis Shannon. Screening the Optical Properties of Ag–Au Alloy Gradients Formed by Bipolar Electrodeposition Using Surface Enhanced Raman Spectroscopy. *Langmuir*, 27(3):878–881, February 2011. Publisher: American Chemical Society.
- [8] Sridevi Ramakrishnan and Curtis Shannon. Display of Solid-State Materials Using Bipolar Electrochemistry. *Langmuir*, 26(7):4602–4606, April 2010. Publisher: American Chemical Society.
- [9] Shinsuke Inagi, Yutaka Ishiguro, Mahito Atobe, and Toshio Fuchigami. Bipolar patterning of conducting polymers by electrochemical doping and reaction. *Angewandte Chemie International Edition*, 49(52):10136–10139, 2010.
- [10] Chunyan Qin, Zhilian Yue, Yunfeng Chao, Robert J Forster, Fionn Ó Maolmhuaidh, Xu-Feng Huang, Stephen Beirne, Gordon G Wallace, and Jun Chen. Bipolar electroactive conducting polymers for wireless cell stimulation. *Applied Materials Today*, 21:100804, 2020.

Sample (I (mA))	position x'_n (cm)	density j (mA/cm ²)	porosity p	thickness d (μ m)	rate v (nm/s)	
$S_1(5)$	0.2	$3.61^{+0.01}_{-0.03}$	0.56 ± 0.03	0.381 ± 0.021	1.52 ± 0.08	
	0.4	$3.36^{+0.09}_{-0.11}$	0.59 ± 0.02	0.403 ± 0.014	1.61 ± 0.06	
	0.6	$2.88^{+0.13}_{-0.14}$	0.58 ± 0.02	0.342 ± 0.015	1.37 ± 0.06	
	0.8	$2.32^{+0.14}_{-0.14}$	0.57 ± 0.02	0.278 ± 0.011	1.11 ± 0.04	
	1.0	$1.80^{+0.13}_{-0.12}$	0.56 ± 0.02	0.224 ± 0.009	0.90 ± 0.03	
	1.2	$1.37^{+0.10}_{-0.09}$	0.56 ± 0.02	0.190 ± 0.007	0.76 ± 0.03	
	1.4	$1.06^{+0.07}_{-0.06}$	0.56 ± 0.02	0.153 ± 0.005	0.61 ± 0.02	
	1.6	$0.83^{+0.05}_{-0.04}$	0.56 ± 0.02	0.124 ± 0.004	0.50 ± 0.02	
	$S_2(10)$	0.2	$7.22^{+0.03}_{-0.07}$	0.64 ± 0.04	0.686 ± 0.054	2.74 ± 0.22
		0.4	$6.72^{+0.02}_{-0.21}$	0.64 ± 0.02	0.694 ± 0.025	2.78 ± 0.10
0.6		$5.77^{+0.27}_{-0.28}$	0.64 ± 0.03	0.592 ± 0.037	2.37 ± 0.15	
0.8		$4.64^{+0.28}_{-0.28}$	0.62 ± 0.03	0.530 ± 0.034	2.12 ± 0.14	
1.0		$3.60^{+0.25}_{-0.23}$	0.61 ± 0.03	0.470 ± 0.027	1.88 ± 0.11	
1.2		$2.75^{+0.19}_{-0.18}$	0.60 ± 0.03	0.414 ± 0.026	1.66 ± 0.10	
1.4		$2.11^{+0.14}_{-0.13}$	0.59 ± 0.03	0.350 ± 0.018	1.40 ± 0.07	
1.6		$1.67^{+0.10}_{-0.09}$	0.58 ± 0.02	0.302 ± 0.014	1.21 ± 0.05	
$S_3(20)$		0.2	$14.45^{+0.06}_{-0.14}$	0.69 ± 0.03	1.208 ± 0.047	4.83 ± 0.19
		0.4	$13.44^{+0.35}_{-0.41}$	0.72 ± 0.02	1.205 ± 0.057	4.82 ± 0.23
	0.6	$11.54^{+0.53}_{-0.55}$	0.71 ± 0.03	1.050 ± 0.058	4.20 ± 0.23	
	0.8	$9.29^{+0.57}_{-0.55}$	0.64 ± 0.06	0.766 ± 0.088	3.06 ± 0.35	
	1.0	$7.20^{+0.49}_{-0.47}$	0.63 ± 0.04	0.540 ± 0.037	2.16 ± 0.15	
	1.2	$5.50^{+0.38}_{-0.36}$	0.61 ± 0.04	0.449 ± 0.035	1.80 ± 0.14	
	1.4	$4.22^{+0.28}_{-0.26}$	0.59 ± 0.03	0.369 ± 0.018	1.48 ± 0.07	
	1.6	$3.33^{+0.19}_{-0.17}$	0.59 ± 0.02	0.338 ± 0.014	1.35 ± 0.06	

Table 2

Current density and fitted parameters for several positions on three samples: porosity, thickness, and etching rate.

- [11] Yutaka Ishiguro, Shinsuke Inagi, and Toshio Fuchigami. Gradient doping of conducting polymer films by means of bipolar electrochemistry. *Langmuir*, 27(11):7158–7162, 2011.
- [12] Michael J Sailor. *Porous Silicon in Practice: Preparation, Characterization and Applications*. John Wiley & Sons, Weinheim, Ger, 2012.
- [13] D Nanda Kumar, Nofar Pinker, and Giorgi Shtenberg. Porous Silicon fabry perot interferometer for N-Acetyl- β -D-Glucosaminidase biomarker monitoring. *ACS sensors*, 5(7):1969–1976, 2020.
- [14] Victor S.-Y. Lin, Kianoush Moteshareh, Keiki-Pua S. Dancil, Michael J. Sailor, and M. Reza Ghadiri. A Porous Silicon-Based Optical Interferometric Biosensor. *Science*, 278(5339):840–843, October 1997. Publisher: American Association for the Advancement of Science Section: Report.
- [15] Keiki-Pua S. Dancil, Douglas P. Greiner, and Michael J. Sailor. A Porous Silicon Optical Biosensor: Detection of Reversible Binding of IgG to a Protein A-Modified Surface. *Journal of the American Chemical Society*, 121(34):7925–7930, September 1999. Publisher: American Chemical Society.
- [16] Lizeth Martínez, David Becerra, and Vivechana Agarwal. Dual layer ZnO configuration over nanostructured porous Silicon substrate for enhanced memristive switching. *Superlattices and Microstructures*, 100:89–96, 2016.
- [17] J Octavio Estevez and Vivechana Agarwal. Porous Silicon photonic crystals. *Handbook of Porous Silicon*, pages 1–10, 2014.
- [18] Rehab Ramadan, Vicente Torres-Costa, and Raúl J Martín-Palma. Fabrication of Zinc Oxide and nanostructured porous Silicon composite micropatterns on Silicon. *Coatings*, 10(6):529, 2020.
- [19] Fereydoon Namavar, Nader M. Kalkhoran, and H. Paul Maruska. Optoelectronic switching and display device with porous silicon. US Patent No. US5272355A, December 1993.
- [20] N. G. Galkin and D. T. Yan. Mechanisms of visible electroluminescence in diode structures on the basis of porous silicon: A review. *Optics and Spectroscopy*, 122(6):919–925, June 2017.
- [21] Bernard Gelloz. Electroluminescence of Porous Silicon. In Leigh Canham, editor, *Handbook of Porous Silicon*, pages 487–499. Springer International Publishing, Cham, 2018.
- [22] JS Pérez-Huerta, D Ariza-Flores, R Castro-García, WL Mochán, GP Ortiz, and V Agarwal. Reflectivity of 1D photonic crystals: A comparison of computational schemes with experimental results. *International Journal of Modern Physics B*, 32(11):1850136, 2018.
- [23] A. David Ariza-Flores, L. M. Gaggero-Sager, and V. Agarwal. White metal-like omnidirectional mirror from porous silicon dielectric multilayers. *Applied Physics Letters*, 101(3):031119, July 2012. Publisher: American Institute of Physics.
- [24] M. Ghulinyan, C. J. Oton, Z. Gaburro, P. Bettotti, and L. Pavesi. Porous silicon free-standing coupled microcavities. *Applied Physics Letters*,

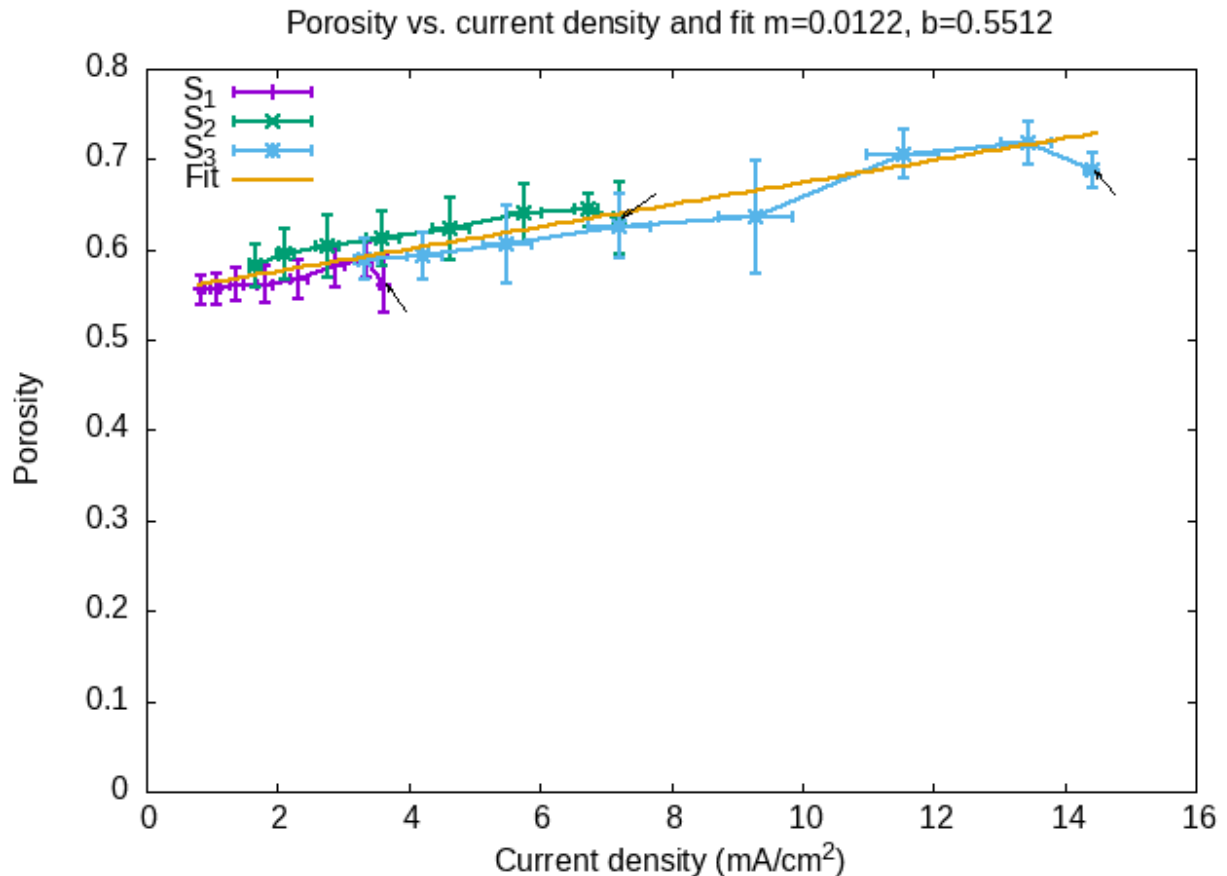


Figure 11: Porosity vs. current density for the three samples S_1 , S_2 , S_3 . The arrows point to data that correspond to position $x'_1 = 0.2$ cm (see text). We include a linear fit of the form $p = mj_{\perp} + b$ with parameters $m = (0.0122 \pm 0.001) \frac{\text{cm}^2}{\text{mA}}$ and $b = 0.551 \pm .005$.

82(10):1550–1552, March 2003. Publisher: American Institute of Physics.

- [25] P. Girault, P. Azuelos, N. Lorrain, L. Poffo, J. Lemaitre, P. Pirasteh, I. Hardy, M. Thual, M. Guendouz, and J. Charrier. Porous silicon micro-resonator implemented by standard photolithography process for sensing application. *Optical Materials*, 72:596–601, October 2017.
- [26] YL Khung, G Barritt, and NH Voelcker. Using continuous porous Silicon gradients to study the influence of surface topography on the behaviour of neuroblastoma cells. *Experimental Cell Research*, 314(4):789–800, 2008.
- [27] Lauren R Clements, Peng-Yuan Wang, Frances Harding, Wei-Bor Tsai, Helmut Thissen, and Nicolas H Voelcker. Mesenchymal stem cell attachment to peptide density gradients on porous Silicon generated by electrografting. *physica status solidi (a)*, 208(6):1440–1445, 2011.
- [28] Leigh Canham. Routes of Formation for Porous Silicon. In Leigh Canham, editor, *Handbook of Porous Silicon*, pages 3–11. Springer International Publishing, Cham, 2018.
- [29] Boyce E Collins, K-PS Dancil, Gaurav Abbi, and Michael J Sailor. Determining protein size using an electrochemically machined pore gradient in Silicon. *Advanced Functional Materials*, 12(3):187–191, 2002.
- [30] Yang Yang Li, Peter Kim, and Michael J Sailor. Painting a rainbow on Silicon: A simple method to generate a porous Silicon band filter gradient. *physica status solidi (a)*, 202(8):1616–1618, 2005.
- [31] Christian R Ocier, Neil A Krueger, Weijun Zhou, and Paul V Braun. Tunable visibly transparent optics derived from porous Silicon. *ACS Photonics*, 4(4):909–914, 2017.
- [32] Neil A Krueger, Aaron L Holsteen, Qiujie Zhao, Seung-Kyun Kang, Christian R Ocier, Weijun Zhou, Glennys Mensing, John A Rogers, Mark L Brongersma, and Paul V Braun. Electrochemical fabrication of flat, polymer-embedded porous Silicon 1d gradient refractive index microlens arrays. *physica status solidi (a)*, 215(13):1800088, 2018.
- [33] Joanna Wang, Michael J Sailor, and Byoung Yong Chang. Fabrication of a lateral gradient rugate in porous Silicon for a miniature spectrometer application. *ChemElectroChem*, 6(24):5967–5972, 2019.
- [34] John David Jackson. *Classical Electrodynamics*. Wiley, New York, NY, 2nd ed. edition, 1975.
- [35] P. P. Ewald. The calculation of optical and electrostatic grid potential. *Annalen Der Physik*, 64(3):253–287, February 1921. Place: Weinheim

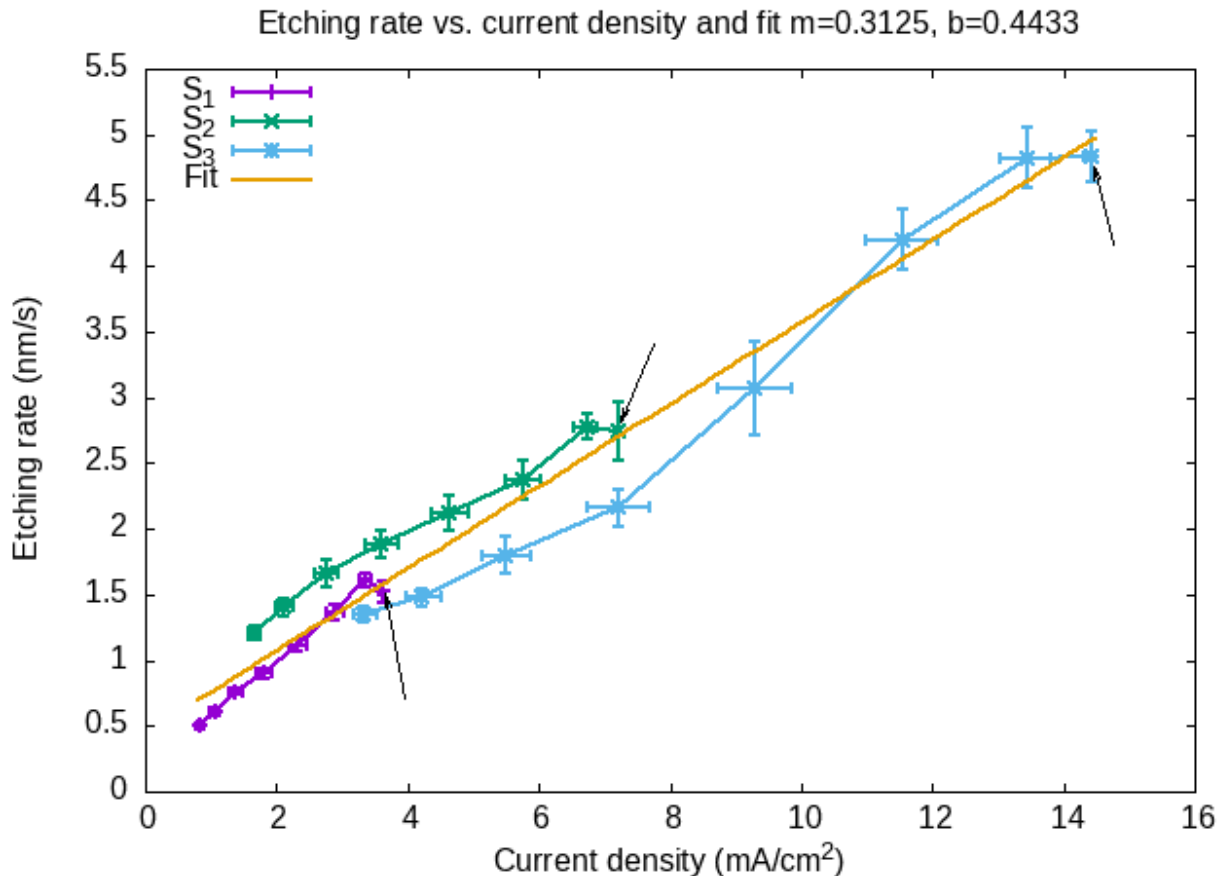


Figure 12: Etching rate vs. current density for three samples S_1 , S_2 , S_3 . The arrows point to data that correspond to position $x'_1 = 0.2$ cm (see text). We include a linear fit of the form $v = mj_{\perp} + b$ to the data with parameters $m = (0.312 \pm 0.017)(\text{cm}^2/\text{mA})(\text{nm}/\text{s})$ and $b = (0.44 \pm 0.09)\text{nm}/\text{s}$.

Publisher: Wiley-VCH Verlag GmbH WOS:000201909400003.

- [36] M. Belhadj, He Alper, and Rm Levy. Molecular-dynamics simulations of water with Ewald summation for the long-range electrostatic interactions. *Chemical Physics Letters*, 179(1-2):13–20, April 1991. Place: Amsterdam Publisher: Elsevier Science Bv WOS:A1991FH14300003.
- [37] K. E. Schmidt and M. A. Lee. Multipole Ewald sums for the fast multipole method. *Journal of Statistical Physics*, 89(1-2):411–424, October 1997. Place: New York Publisher: Plenum Publ Corp WOS:A1997YJ02200025.
- [38] A. Grzybowski, E. Gwozdz, and A. Brodka. Ewald summation of electrostatic interactions in molecular dynamics of a three-dimensional system with periodicity in two directions. *Physical Review B*, 61(10):6706–6712, March 2000. Place: College Pk Publisher: Amer Physical Soc WOS:000085985800038.
- [39] Abdunour Toukmaji, Celeste Sagui, John Board, and Tom Darden. Efficient particle-mesh Ewald based approach to fixed and induced dipolar interactions. *The Journal of Chemical Physics*, 113(24):10913–10927, December 2000. Publisher: American Institute of Physics.
- [40] A. Bródka. Ewald summation method with electrostatic layer correction for interactions of point dipoles in slab geometry. *Chemical Physics Letters*, 400(1-3):62–67, December 2004. Place: Amsterdam Publisher: Elsevier Science Bv WOS:000225679200013.
- [41] Salvatore Campione and Filippo Capolino. Ewald method for 3D periodic dyadic Green's functions and complex modes in composite materials made of spherical particles under the dual dipole approximation. *Radio Science*, 47:RS0N06, September 2012. Place: Washington Publisher: Amer Geophysical Union WOS:000316957000001.
- [42] B. R. A. Nijboer and F. W. De Wette. On the calculation of lattice sums. *Physica*, 23(1):309–321, January 1957.
- [43] Bra Nijboer and Fw Dewette. The Internal Field in Dipole Lattices. *Physica*, 24(6):422–431, 1958. Place: Amsterdam Publisher: Elsevier Science Bv WOS:A1958WX86900005.
- [44] F. W. de Wette and G. E. Schacher. Internal Field in General Dipole Lattices. *Physical Review*, 137(1A):A78–A91, January 1965. Publisher: American Physical Society.
- [45] R. E. Watson, J. W. Davenport, M. L. Perlman, and T. K. Sham. Madelung effects at crystal surfaces: Implications for photoemission. *Physical Review B*, 24(4):1791–1797, August 1981. Publisher: American Physical Society.

R vs j_{\perp} and λ (t=250s)

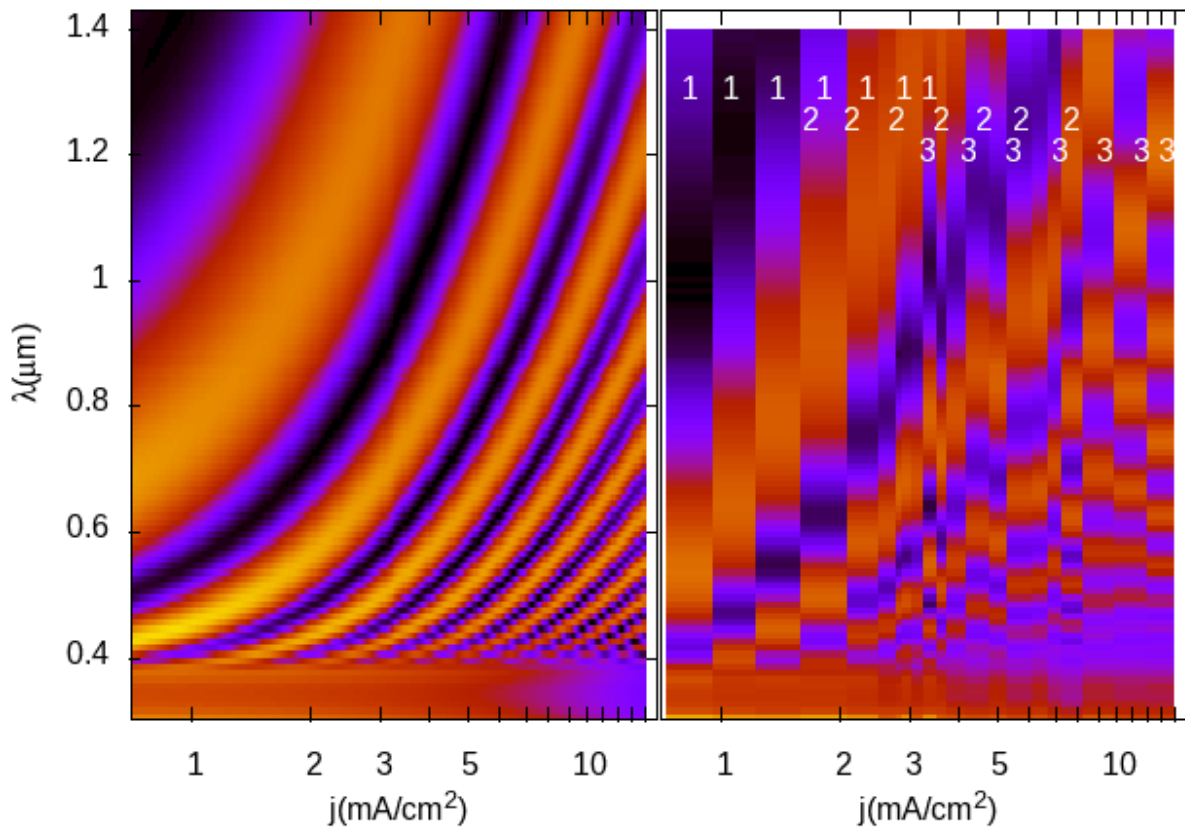


Figure 13: Reflection R of a PS film as a function of the current density current j_{\perp} and wavelength λ for an etching time $t = 250$ s. Theory (left panel) and experiment (right panel, see text). We indicate with the numbers 1, 2, 3 the data corresponding to the corresponding samples S_1 , S_2 (shifted, see text) and S_3 .

- [46] J. Grindlay. On the K-dependence of the electrical field in a crystalline slab of oscillating charges. *Canadian Journal of Physics*, July 1981. Publisher: NRC Research Press Ottawa, Canada.
- [47] Olaf Stenzel et al. *The Physics of Thin Film Optical Spectra*. Springer, Jena, Ger, 2015.
- [48] Klaus D Sattler. *Silicon Nanomaterials Sourcebook: Low-Dimensional Structures, Quantum Dots, and Nanowires*, volume One. CRC Press, Boca Raton, FL, 2017.
- [49] Wolfgang Theiß. Optical properties of porous Silicon. *Surface Science Reports*, 29(3-4):91–192, 1997.
- [50] Leandro L. Missoni, Guillermo P. Ortiz, María Luz Martínez Ricci, Victor J. Toranzos, and W. Luis Mochán. Rough 1D photonic crystals: A transfer matrix approach. *Optical Materials*, 109:110012, November 2020.